ICSV 21
13-17 July, 2014, Beijing/China

The 21st International Congress on Sound and Vibration

13-17 July, 2014, Beijing/China

AERODYNAMIC NOISE FROM A TRAIN PANTOGRAPH

Xiaowan Liu[1], David Thompson[1], Zhiwei Hu[1], Vincent Jurdic[2]

[1]*Institute of Sound and Vibration Research, University of Southampton, SO17 1BJ, UK*

[2]*Arup Acoustics, 8 St Thomas St, Winchester, SO23 9HE, UK*

e-mail: xl25g11@soton.ac.uk

Many studies have shown that when the speed of high speed trains exceeds around 300km/h, aerodynamic noise becomes the most significant noise source. The pantograph, or current collector, is mounted on the top of the train and is therefore not shielded by noise barriers. This study is focused on pantograph noise reduction using a computational approach. Due to the complex geometry of the pantograph and the fact that it is composed of a number of slender bodies, a component-based approach is adopted to ensure the feasibility of numerical simulations. Computational Fluid Dynamics calculations are carried out using a DDES model. The far-field noise is calculated by using the Ffowcs Williams-Hawkings equation based upon the aerodynamic characteristics obtained in the near-field by the CFD model. The investigation concentrates on the sound generated by a circular cylinder, typical of the pantograph, in cross-flow with various speeds and yaw angles. The simulated aerodynamic results give a commendable agreement with experimental results.

1. Introduction

It is normally assumed that the overall noise from trains can be decomposed into two main components: rolling noise and aerodynamic noise. Aerodynamic noise becomes predominant for speeds above 300 – 350 km/h[1]. The pantograph is known to be one of the main aerodynamic noise sources on high speed trains, especially when noise barriers are built beside the railway. As a result, it is important to achieve reductions of pantograph noise.

A number of pantograph noise studies have been carried out, principally in Japan and in Germany. Kurita et al.[2] carried out microphone array measurements to investigate the noise sources of a PS207 type pantograph. Ikeda and Mitsumoji[3] conducted a numerical simulation based on Howe's vortex sound theory to identify the structure of sound sources around the panhead. Ikeda and Mitsumoji[4] found that the interference between the panhead and its support also induced distinct aerodynamic noise. They studied various configurations of the panhead and its support and evaluated the aerodynamic noise using CFD analysis and Curle's equation. Sueki et al.[5] covered the pantograph component surfaces with particular porous materials. The noise level was found to be reduced by 0.8-1.5dB in wind tunnel measurements, but not in field tests.

Grosche and Meier[6] measured on a full-scale DSA350SEK pantograph in the wind tunnel and found that the strongest noise sources were located at the foot, the panhead and the knee joint. Further detailed study was conducted by Lölgen[7]. For DSA350SEK, he identified the pantograph components corresponding to different peak levels based on the Strouhal number relationship (the Strouhal number *St*, is the non-dimensional frequency given by fD/U where f is the frequency, D is

a typical dimension (here the diameter) and U is the flow velocity). Brick et al.[8] conducted a measurement to study the influence of the turbulent boundary layer of the train roof on the noise generation. They indicated that the turbulence can affect the noise generation of the pantograph recess and the lowered pantograph significantly. Since the pantograph consists of a number of slender bodies, King and Barsikow[9] carried out experiments to investigate the noise generation of yawed cylinders with various cross-sections. They found that the Strouhal number and radiated noise level of a cylinder yawed up to 60° are approximately independent of the yaw angle after being normalized by the velocity component normal to the cylinder. This is called the *Independence Principle*.

Due to the complexity of the pantograph geometry, it is not feasible to perform full scale pantograph simulation. Instead, the detailed pantograph is divided into a number of representative components and the noise from each component is computed separately. Since most components of a pantograph are slender cylinders with different shapes, sizes and alignment and the circular cylinder flow is the most challenging of the bluff body flow studies, the present paper focusses on a study of circular cylinder noise.

The flow around a circular cylinder has been extensively studied. Zdravkovich[10] described comprehensive flow states for a wide range of Reynolds numbers, *Re*. Reynolds number is a dimensionless quantity and expresses the ratio of inertial forces to viscous forces, which can be obtained by UL/υ where υ is the kinematic viscosity. The relationships between the fluctuating lift coefficient C'_l, the time-averaged drag coefficient C_d, the Strouhal number *St* associated with vortex shedding, and the Reynolds number *Re* are illustrated in Figure 1 and Figure 2. Of particular interest to the pantograph case is the critical regime ($1\times10^5 < Re < 4\times10^5$). It is difficult to investigate in both experiments and numerical simulations because of the sensitivity of the transition location. The distinct features for this flow regime are the rapid decrease of the drag coefficient and the presence of an asymmetric pressure distribution on the cylinder surface. This is caused by the fact that the transition from laminar to turbulent flow occurs only on one side of the cylinder. As the pressure fluctuations on the cylinder surface are highly related to noise generation, an accurate prediction of the forces exerted upon the cylinder is essential.

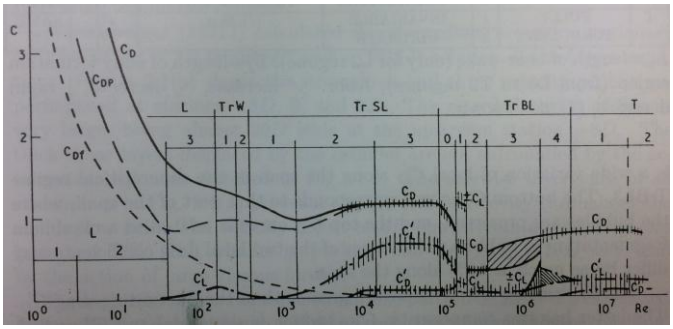

Figure 1. Variation of force coefficients. [10]

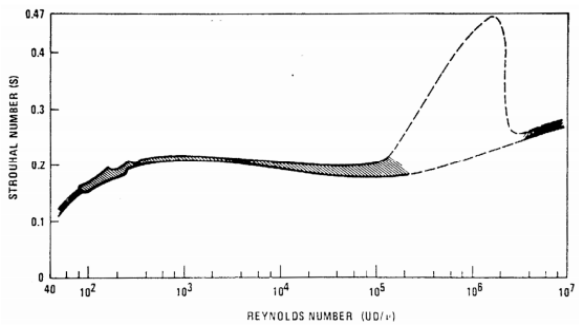

Figure 2. The relationship between *St* and *Re*.[10]

For the pantograph geometry, some circular cylinders, e.g. the pantograph arms, are not perpendicular to the free stream, but have certain yaw angles. This study focuses on investigating aeroacoustic characteristics of circular cylinders in yaw with yaw angles in the range 0° – 75°. The effect of various speeds are also considered. The aeroacoustic problem is solved in two steps. The first step is to obtain an accurate aerodynamic characteristics in the near-field by using a Delayed Detached Eddy Simulation model, while the second step is to predict far-field noise based on the Ffowcs-Williams & Hawkings equation by using aerodynamic information as input.

2. Computational setup

The yawed cylinder geometry and nomenclature are defined in Figure 3. Λ is the yaw angle. The freestream velocity has two components: one is normal to the cylinder axis (*x*-direction), $U_n = U\cos\Lambda$ and the other is parallel to the cylinder axis (*z*-direction), $U_t = U\sin\Lambda$. In order to simplify the grid generation, the arrangement shown in Figure 4 is used. The diameter of the circular cylinder is D=0.05m which is the size of a typical pantograph arm. The computational domain extends over 30D in the *x*-direction, with the centre of the cylinder 20D from the downstream boundary. In the *y*-direction, the domain size is 20D with equal distance to the top and bottom. To simulate cylinders with an infinite span, periodic boundary conditions are applied in the spanwise direction. On the planes $y = \pm 10D$ symmetry boundary conditions are imposed. The boundary surface of the cylinder is set to a no-slip condition. The velocity inlet and pressure outlet conditions are applied to the vertical planes, i.e. $x = -10D$ and $+20D$. The non-dimensional time step size ($U\Delta t/D$) is 0.009 which ensures the maximum Courant number ($U\Delta t/\Delta x$**)** is less than 2. The cases of yawed circular cylinders in present study are listed in Table 1 as well as the computational cost needed. For all cases, the overall values of y^+ (non-dimensional wall distance) around the cylinder surface were checked after the simulation, and found to be lower than 1.

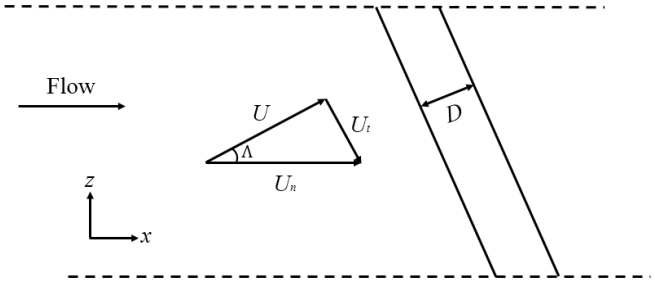

Figure 3. Definition of geometry and nomenclature.

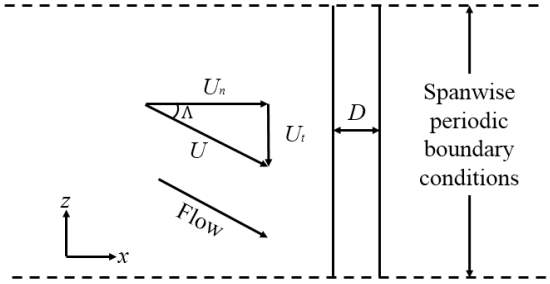

Figure 4. Computational model

Table 1. Summary of cases.

Freestream velocity (U) (Unit:m/s)	Yaw angles (Λ)					Reynolds number	Cells	Computing processors	Computing time
30	0°	30°	45°	60°	75°	1×10^5	1,285,340	96	4 days
60	0°	30°	45°	60°	75°	2×10^5	3,808,220	128	7 days

3. Results

3.1 Grid dependence study

Table 2. Summary of the global flow parameters at U=30m/s, Λ=0°.

Case	Cells	*Re*	$C_{l,rms}$	$C_{d,mean}$	*St*	$-C_{pb}$	L_r/D
Coarse (DDES)	548,550	1×10^5	0.43	1.07	0.20	0.82	0.9
Medium (DDES)	987,450	1×10^5	0.65	1.19	0.19	1.0	0.78
Fine (DDES)	1,285,340	1×10^5	0.75	1.25	0.19	1.1	0.6
Cantwell and Coles[13] (Exp.)	-	1.4×10^5	-	1.24	0.18	1.21	0.5-0.6
Breuer[11] (LES, Case A1)	-	1.4×10^5	-	1.24	0.204	1.4	0.57
Travin et al.[12] (DES)	-	1.4×10^5	0.29	1.08	0.21	1.04	1.1

A grid dependence study was carried out before the effect of yaw angles and flow speeds was investigated. Three types of mesh were used to simulate the infinite circular cylinder in cross-flow

($\Lambda = 0°$) at U=30m/s. Reported in Table 2 are the fluctuating lift coefficient $C_{l,rms}$, time-averaged drag coefficient $C_{d,mean}$, Strouhal number St, separation angle θ_{sep}, base pressure coefficient C_{pb}, and the length of the recirculation zone L_r/D. As the grid is gradually refined, the simulation results tend to approach the experiment, but there is still a difference between various grids, which means that the grid convergence is not achieved. This is consistent with the findings of the LES simulation of Breuer[11] and the DES simulation of Travin et al.[12] at $Re = 1.4\times10^5$. Recall that $1\times10^5 < Re < 4\times10^5$ is the critical regime, where the transition to turbulence happens in the free shear layer towards the separation point. The location of transition can affect other turbulence properties significantly, and it is difficult to predict due to the extreme sensitivity of the transition location. This leads to highly scattered experimental and numerical data. In the present study, the fine mesh provides a commendable agreement with experimental data. Hence the fine grid configuration was applied in the following yawed cylinder cases.

3.2 Yawed circular cylinders at U=30m/s

3.2.1 Aerodynamic results

Table 3 presents some important parameters of which $C_{l,rms}$ and St are significant for aeroacoustic characteristics. The drag and lift forces are normalized by $(0.5\rho U_0^2 DL)$ in which D is the diameter of the cylinder and L is the spanwise length. The parameters denoted by subscript 'n' indicate the values normalized by the normal velocity, $U_n = U\cos\Lambda$. It can be seen that higher Λ leads to significantly reduced amplitudes of the lift force fluctuations. It is expected that with increased yaw angle, the noise level will be reduced. The relationships between $C_{l,rms}$, $C_{d,mean}$, St and the yaw angle, Λ, are plotted in Figure 5. The *Independence Principle* is represented by a factor $\cos^2\Lambda$ in Figure 5(a),(b) and $\cos\Lambda$ in Figure 5(c). The results show that $C_{d,mean}$ and St obey the *Independence Principle* well, but $C_{l,rms}$ fails to follow it.

Table 3. Summary of important parameters for yawed cylinders at U=30m/s.

Λ	Re_n	$C_{l,rms}$	$C_{d,mean}$	f	St
0	1×10^5	0.75	1.25	114	0.19
30	0.87×10^5	0.408	0.867	103	0.172
45	0.71×10^5	0.271	0.576	83	0.139
60	0.5×10^5	0.179	0.312	57	0.095
75	2.6×10^4	0.042	0.082	30	0.05

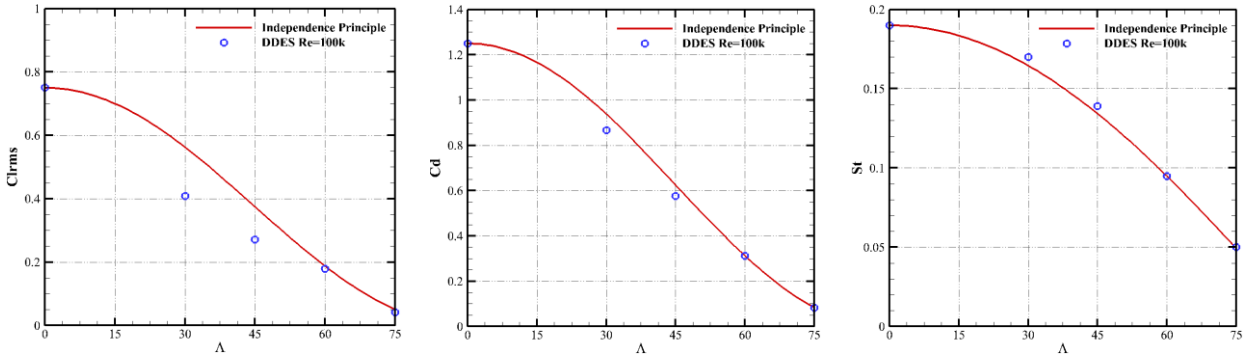

(a) $C_{l,rms}$ vs Λ **(b)** $C_{d,mean}$ vs Λ **(c)** St vs Λ

Figure 5. The relationships between $C_{l,rms}$, $C_{d,mean}$, St and Λ at U=30m/s.

Figure 6 visualizes the wake structures of yawed cylinders at the non-dimensional time $Ut/D = 600$ represented by the iso-surface of normalized Q criterion of 0.1 (coloured by non-dimensional velocity magnitude). The flow past the yawed cylinders exhibits coherent alternating

periodic vortex shedding. The spanwise vortex structures are parallel to the cylinders axis and the streamwise vortex structures are perpendicular to the cylinder axis except for $\Lambda = 60°$ and 75°. For these two angles, both the spanwise and streamwise vortex structures become twisted. In addition, with increased yaw angle, the vortex structures disappear in the downstream region and it can be expected that the noise levels may reduce.

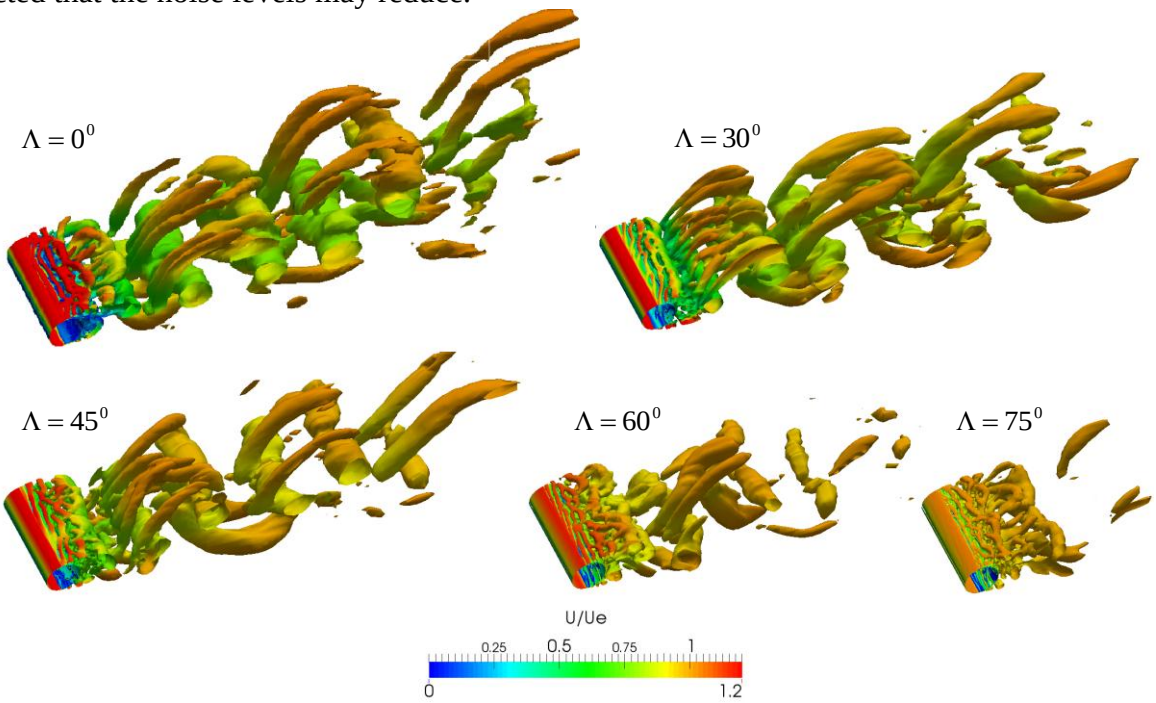

Figure 6. Instantaneous normalized Q criterion for yawed cylinders.

3.2.2 Aeroacoustic results

After obtaining aerodynamic characteristics in the near-field, the aerodynamic noise was calculated by the FW-H equation without considering the convective effects. The pressure fluctuations on the cylinder surface used as input for the acoustic calculation were sampled from $Ut/D = 540$ to 900. The sound pressure spectrum at the receivers, which are 5m away from the cylinder axis at $\theta = 90°$ and 180°, are shown in Figure 7. θ is determined clockwise from the leading edge of the cylinder. In Figure 7, an Aeolian tone is apparent for each yaw angle which is associated with the vortex shedding frequency. The peak frequency at $\theta = 180°$ for each yaw angle is nearly twice that at $\theta = 90°$, and the overall sound pressures at $\theta = 180°$ are much lower than that at $\theta = 90°$. This is due to the fact that the receiver at $\theta = 180°$ is mainly influenced by the fluctuating drag force, while at $\theta = 90°$, it is mainly influenced by the fluctuating lift force. With increased yaw angle, the noise level is reduced and accompanied with a decrease of the peak frequency. This is consistent with the previous aerodynamic findings.

In Figure 8, the noise directivity is plotted for each yaw angle based on the overall sound pressure level at the far-field receivers, which are located in the plane parallel to the incoming flow direction at a radial distance $R = 100D = 5$m from the cylinder axis. The overall sound pressure level is obtained by integrating over a limited frequency range, up to a certain cut-off frequency where the minimum level occurs. The noise levels at higher frequencies are artefacts caused by the coarse spatial resolution and are therefore neglected. A dipole directivity pattern is predicted for each yaw angle. As no convective effects are considered, the dipole pattern is axisymmetric along the *x*-, and *y*-axis. For each yaw angle, the maxima of the SPL are located at $\theta = 90°$, 270° and the minima at $\theta = 0°$, 180°. With increased yaw angle, the difference of SPL between maxima and minima becomes larger; it is in the range of 15-25dB. Figure 9 shows the relationships between ΔSPL and Λ

at different receivers where ΔSPL is the SPL generated by the yawed cylinders minus the SPL produced by the unyawed cylinder. Between Λ = 0° and 75° at $\theta = 180°$ ΔSPL is nearly 27dB whereas at $\theta = 90°$ it is 36dB. The reduction of SPL can fit the curve of 60logcosΛ at $\theta = 90°$, while at $\theta = 180°$ it is close to 50logcosΛ.

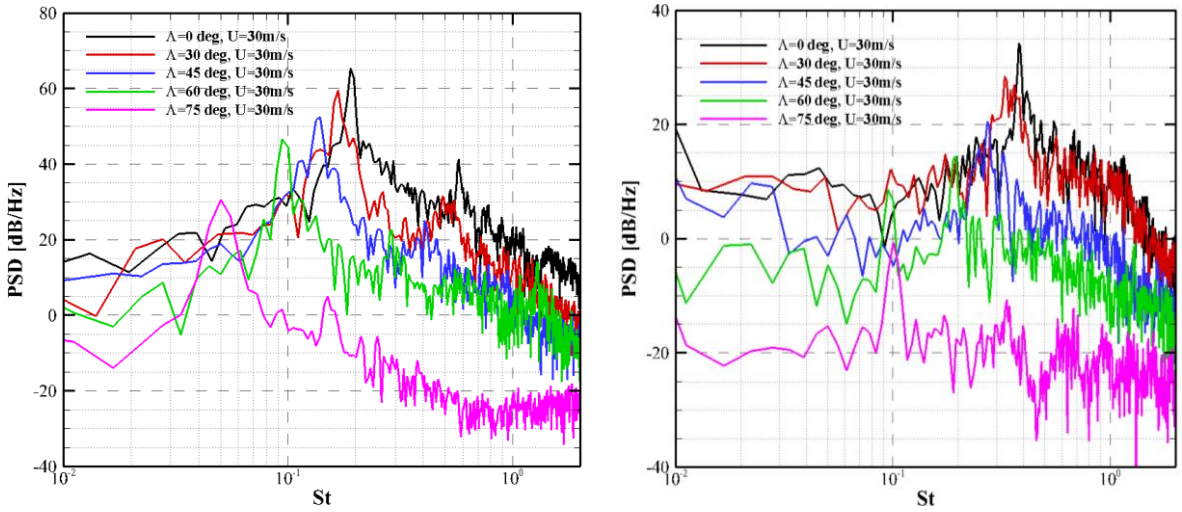

(a) $\theta = 90^0$ **(b)** $\theta = 180^0$

Figure 7. Noise spectra for yawed cylinders at *U*=30m/s and *R*=5m.

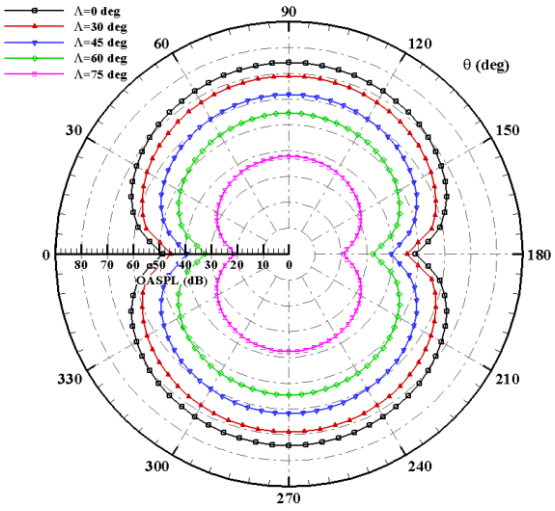

Figure 8. OASPL directivity of yawed cylinders at U=30m/s and R=5m

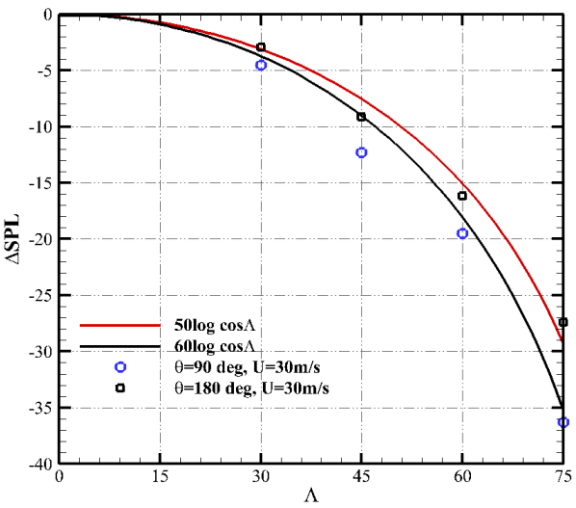

Figure 9. ΔSPL as a function of yaw angle at 30m/s

3.3 Yawed circular cylinders at U=60m/s

3.3.1 Aerodynamic results

For 60m/s, the important parameters are summarized in Table 5. Compared to the results for 30m/s, $C_{d,mean}$ and $C_{l,rms}$ are significantly lower while *St* increases slightly for each yaw angle. This due to the fact that the Reynolds numbers at 30m/s and 60m/s for Λ = 0° lie in the transitional flow regime. The remarkable feature of this regime is the considerable variations of force coefficients which have been illustrated in Figure 1 and Figure 2. The other interesting feature observed is the asymmetric pressure distribution around the cylinder surface which is accompanied with different separation angles between the upper and lower sides of the cylinder. This phenomenon is consistent with experiment and LES simulation. Due to the extreme sensitivity of the transition location, it is quite difficult to predict the turbulence characteristics properly. However, $C_{d,mean}$, $C_{l,rms}$ and *St* ob-

tained from the present simulation agree well with experiment. The relationships between these quantities and Λ are given in Figure 10. Compared to Figure 5, all these parameters fit the curve of the *Independence Principle* better.

Table 4. Summary of important parameters for yawed cylinders at U=60m/s

Λ	Re_n	$C_{l,rms}$	$C_{d,mean}$	f	St
0	2×10^5	0.08	0.69	305	0.254
30	1.7×10^5	0.07	0.52	264	0.22
45	1.4×10^5	0.045	0.344	210	0.179
60	1×10^5	0.033	0.17	150	0.125
75	5.2×10^4	0.0068	0.036	90	0.075

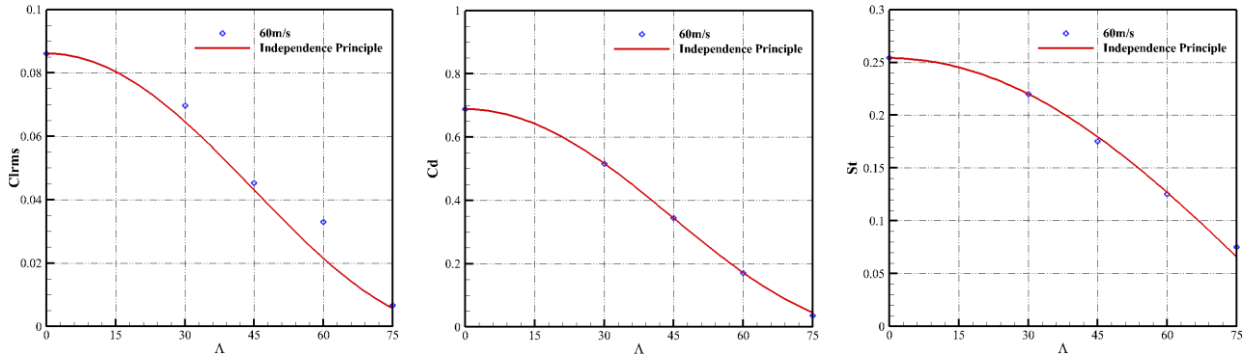

(d) $C_{l,rms}$ vs Λ **(e)** $C_{d,mean}$ vs Λ **(f)** St vs Λ

Figure 10. The relationships between $C_{l,rms}$, $C_{d,mean}$, St and Λ at U=60m/s.

3.3.2 Aeroacoustic results

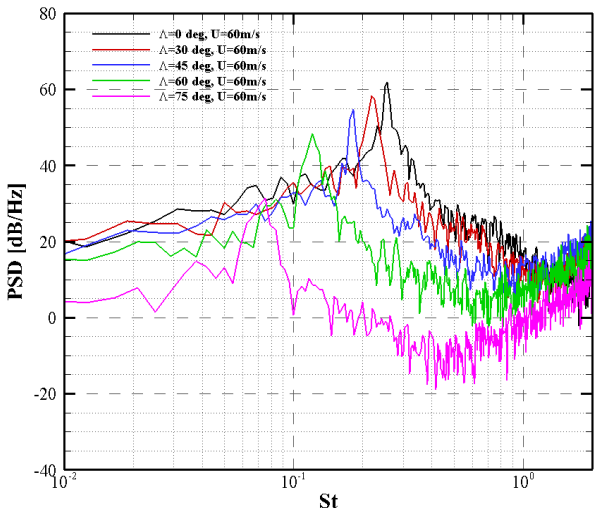

Figure 11. Noise spectra for yawed cylinders at U=60m/s and R=5m

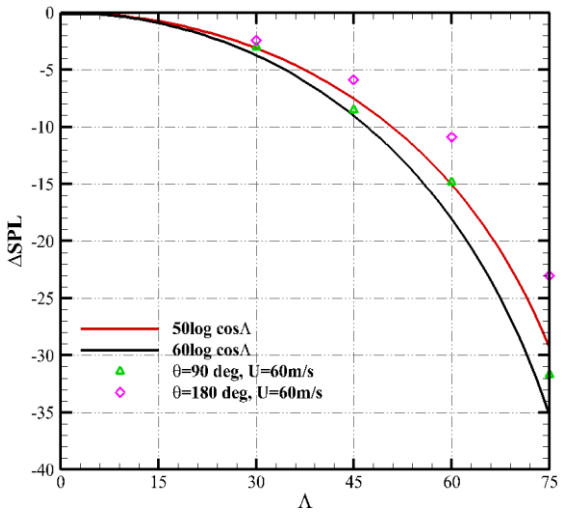

Figure 12. ΔSPL as a function of yaw angle at 60m/s

The sound pressure spectra at the receivers which are 5m away from the cylinder axis at $\theta = 90°$ are shown in Figure 11. Compared to Figure 7(a), the dominant peak frequency exhibited for each yaw angle are slightly higher which is related to the delayed eddy formation. With increased yaw angle, the difference of peak level between 30m/s and 60m/s becomes more conspicuous. In addition, a dipole directivity pattern is again predicted for 60m/s which is similar to that of 30m/s. Figure 12 shows the relationships between ΔSPL and Λ. At $\theta = 90°$, ΔSPL is in the range between 50logcosΛ and 60logcosΛ, while at $\theta = 180°$ it exceeds this range. The difference in SPL

between the two speeds at the same receiver increases gradually with higher yaw angle. At $\theta = 90°$, the lowest difference is 1dB at $\Lambda = 0°$ and the highest difference is 5.6dB at $\Lambda = 75°$.

4. Conclusions

In the present study, the noise characteristics of circular cylinders in yaw were investigated numerically considering the effect of various yaw angles and speeds. A higher yaw angle leads to reduced $C_{d,mean}$, $C_{l,rms}$ and *St*. The *Independence Principle* is not followed for $C_{l,rms,}$ but works well for $C_{d,\text{mean}}$ and *St.* A dipole directivity pattern is exhibited for each yaw angle. A strong correlation between the far-field noise and the yaw angle was observed. With increased yaw angle, both the level and frequency of the peak reduces. These features are closely related to the force fluctuations on the cylinder surface and the vortex shedding frequency. With higher speed, the peak frequency increase slightly which is caused by the delayed eddy formation. The difference in sound pressure level between the two speeds becomes greater with higher yaw angle.

REFERENCES

1. Thompson, D. *Railway noise and vibration: mechanisms, modelling and means of control*. Elsevier, (2008).
2. Kurita, T., Hara, M., Yamada, H., Wakabayashi, Y., Mizushima, F., Satoh, H., & Shikama, T. Reduction of pantograph noise of high-speed trains, *Journal of Mechanical systems for Transportation and Logistics*, *3*, 63-74, (2010).
3. Ikeda, M., & Mitsumoji, T. Evaluation Method of Low-Frequency Aeroacoustic Noise Source Structure Generated by Shinkansen Pantograph, *Quarterly Report of RTRI*, *49*(3), 184-190, (2008).
4. Ikeda, M., & Mitsumoji, T. Numerical Estimation of Aerodynamic Interference between Pan-head and Articulated Frame, *Quarterly Report of RTRI*, *50*(4), (2009).
5. Sueki, T., Ikeda, M., Takaishi, T., Kurita, T., & Yamada, H. Reduction of aerodynamic noise from high-speed pantograph using porous materials, *Journal of Environment and Engineering*, *5*(3), 469-484, (2010).
6. Grosche, F. R., & Meier, G. E. A. Research at DLR Göttingen on bluff body aerodynamics, drag reduction by wake ventilation and active flow control, *Journal of Wind Engineering and Industrial Aerodynamics*, *89*(14), 1201-1218, (2001).
7. Lölgen, T. Wind tunnel noise measurements on full-scale pantograph models, *The Journal of the Acoustical Society of America*, *105*(2), 1136-1136, (1999).
8. Brick, H., Kohrs, T., Sarradj, E. and Geyer, T. Noise from high-speed trains: Experimental determination of the noise radiation of the pantograph, in *Forum Acusticum*, (2011).
9. King, W.F., & Barsikow, B. Deufrako K2 report, An experimental study of sound generated by flow interactions with free-ended cylinders, (1997).
10. Zdravkovich, M. M. *Flow around Circular Cylinders: Volume 1: Fundamentals*. Oxford University Press, (1997).
11. Breuer, M. A challenging test case for large eddy simulation: high Reynolds number circular cylinder flow, *International Journal of Heat and Fluid Flow*, *21*(5), 648-654, (2000).
12. Travin, A., Shur, M., Strelets, M., & Spalart, P. Detached-eddy simulations past a circular cylinder, *Flow, Turbulence and Combustion*, *63*(1-4), 293-313, (2000).
13. Cantwell, B., & Coles, D. An experimental study of entrainment and transport in the turbulent near wake of a circular cylinder, *Journal of Fluid Mechanics*, *136*, 321-374, (1983).